A More Accurate Transonic Computational Method for Wing-Body Configurations

L. T. Chen*
McDonnell Douglas Corporation, St. Louis, Missouri

Second- and third-order, quasiconservative and fully conservative schemes have been developed for computing inviscid flowfields about transonic wings. The fully conservative schemes are developed by modifying an existing finite volume algorithm, while the quasiconservative schemes are developed by solving a transformed full-potential equation with the addition of new second- or third-order artificial viscosities at supersonic points. A new shock-point operator is introduced, which adjusts the amount of nonconservative differencing at shock points and thus modifies the location and strength of captured shocks. Numerical results obtained using the second- and third-order schemes will be discussed and compared with experimental data.

Introduction

MOST existing schemes[1-5] available for computing transonic potential flowfields about wings or wing-body combinations are limited to first-order accuracy in supersonic regions because of the use of first-order upwind differencing or the addition of first-order artificial viscosities or densities. Although the schemes have been used extensively for preliminary aerodynamic design, most of their successful applications are limited to simple wing-body geometries. Extension to more complex geometries is prohibited by the need for a large number of grid points for adequate prediction of shock location and strength, especially for predicting double shocks which are common features of flows about highly swept and aft-cambered wings. Development of higher order schemes, therefore, is necessary to improve the resolution of solutions for realistic wing-body geometries with a reasonable number of grid points.

Several second-order schemes[6-9] have been introduced for airfoil and cascade flowfield calculations. Jameson[10] and Chen[7] demonstrated that second-order fully conservative and quasiconservative schemes, respectively, are capable of predicting double shocks on an airfoil surface which cannot be resolved accurately using a first-order scheme without a large number of grid points. Chen[7] also demonstrated that his second-order quasiconservative scheme provides better resolution of a double shock than the second-order fully conservative scheme. Ives and Liutermoza[8] showed that their second-order nonconservative scheme provides better resolution for transonic cascade flows than first-order nonconservative schemes. A discussion of first- and second-order nonconservative schemes also has been given in Ref. 7. A fundamental study of artificial viscosities and shock-point operators of different orders was provided in Ref. 11 by Chen and Caughey, and a third-order quasiconservative scheme was also introduced there. The third-order quasiconservative solutions were found to be essentially no different from the second-order quasiconservative solutions for airfoil applications.

In the present study, second- and third-order, fully conservative and quasiconservative schemes are developed for computing flowfields about transonic wings. To the author's knowledge, this is the first demonstration of successful third-order schemes and, also, the first presentation of both second- and third-order solutions for transonic potential flowfield computations about wings or wing-body combinations.

Presented as Paper 82-0162 at the AIAA 20th Aerospace Sciences Meeting, Orlando, Fla., Jan. 11-14, 1982; submitted Jan. 22, 1982; revision received Sept. 7, 1982.

*Scientist, McDonnell Douglas Research Laboratories; currently Senior Engineer-Scientist, Douglas Aircraft Company, Long Beach. Member AIAA.

Full Potential Equation

Quasiconservative schemes solve finite difference approximations of the full potential equation. Therefore, it is convenient to formulate the full potential equation first in computational coordinates. By applying the chain rule, derivatives of the potential function ϕ in physical coordinates (x,y,z) can be related to its derivatives in an arbitrary curvilinear coordinate system (X,Y,Z) as follows.

$$\begin{bmatrix} \phi_x \\ \phi_y \\ \phi_z \end{bmatrix} = A \begin{bmatrix} \phi_X \\ \phi_Y \\ \phi_Z \end{bmatrix} \tag{1}$$

$$\begin{bmatrix} \phi_{xx} \\ \phi_{yy} \\ \phi_{xy} \\ \phi_{zz} \\ \phi_{xz} \\ \phi_{yz} \end{bmatrix} = -BCA \begin{bmatrix} \phi_X \\ \phi_Y \\ \phi_Z \end{bmatrix} + B \begin{bmatrix} \phi_{XX} \\ \phi_{YY} \\ \phi_{XY} \\ \phi_{ZZ} \\ \phi_{XZ} \\ \phi_{YZ} \end{bmatrix} \tag{2}$$

where

$$A = \begin{bmatrix} x_X & y_X & z_X \\ x_Y & y_Y & z_Y \\ x_Z & y_Z & z_Z \end{bmatrix}^{-1} \tag{3}$$

$$B = \begin{bmatrix} x_X^2 & y_X^2 & 2x_Xy_X & z_X^2 & 2x_Xz_X & 2y_Xz_X \\ x_Y^2 & y_Y^2 & 2x_Yy_Y & z_Y^2 & 2x_Yz_Y & 2y_Yz_Y \\ x_Xx_Y & y_Xy_Y & x_Xy_Y+x_Yy_X & z_Xz_Y & x_Xz_Y+x_Yz_X & y_Xz_Y+y_Yz_X \\ x_Z^2 & y_Z^2 & 2x_Zy_Z & z_Z^2 & 2x_Zz_Z & 2y_Zz_Z \\ x_Xx_Z & y_Xy_Z & x_Xy_Z+x_Zy_X & z_Xz_Z & x_Xz_Z+x_Zz_X & y_Xz_Z+y_Zz_X \\ x_Yx_Z & y_Yy_Z & x_Yy_Z+x_Zy_Y & z_Yz_Z & x_Yz_Z+x_Zz_Y & y_Yz_Z+y_Zz_Y \end{bmatrix}^{-1} \tag{4}$$

$$C=\begin{bmatrix} x_{XX} & x_{YY} & x_{XY} & x_{ZZ} & x_{XZ} & x_{YZ} \\ y_{XX} & y_{YY} & y_{XY} & y_{ZZ} & y_{XZ} & y_{YZ} \\ z_{XX} & z_{YY} & z_{XY} & z_{ZZ} & z_{XZ} & z_{YZ} \end{bmatrix}^T \tag{5}$$

and the full potential equation to be solved is

$$(a^2-u^2)\phi_{xx}+(a^2-v^2)\phi_{yy}+(a^2-w^2)\phi_{zz}-2uv\phi_{xy} -2vw\phi_{yz}-2uw\phi_{xz}=0 \tag{6}$$

where u,v,w are the x,y,z components of the flow velocity, respectively, and a is the local speed of sound determined from the energy equation

$$a^2=a_0^2-[(\gamma-1)/2](u^2+v^2+w^2) \tag{7}$$

where γ is the ratio of specific heats for the assumed calorically perfect gas and a_0 the stagnation speed of sound.

Substituting Eqs. (1) and (2) into Eq. (6) and performing matrix inversion, multiplication, and careful algebraic manipulation, a full potential equation multiplied by the determinant of the Jacobian transformation matrix D can be derived in arbitrary curvilinear coordinates as

$$c_1\phi_{XX}+c_2\phi_{YY}+c_3\phi_{ZZ}+c_4\phi_{XY}+c_5\phi_{YZ}+c_6\phi_{XZ}+c_7\phi_X +c_8\phi_Y+c_9\phi_Z=0 \tag{8}$$

where

$$c_1=[a^2(h_1^2+h_2^2+h_3^2)-U^2]/D \tag{9a}$$

$$c_2=[a^2(h_4^2+h_5^2+h_6^2)-V^2]/D \tag{9b}$$

$$c_3=[a^2(h_7^2+h_8^2+h_9^2)-W^2]/D \tag{9c}$$

$$c_4=[2a^2(h_1h_4+h_2h_5+h_3h_6)-2UV]/D \tag{9d}$$

$$c_5=[2a^2(h_4h_7+h_5h_8+h_8h_9)-2VW]/D \tag{9e}$$

$$c_6=[2a^2(h_1h_7+h_2h_8+h_3h_9)-2UW]/D \tag{9f}$$

$$c_7=(h_1p_X+h_2p_Y+h_3p_Z)/D \tag{9g}$$

$$c_8=(h_4p_X+h_5p_Y+h_6p_Z)/D \tag{9h}$$

$$c_9=(h_7p_X+h_8p_Y+h_9p_Z)/D \tag{9i}$$

U,V,W are velocity components defined as

$$U=h_1u+h_2v+h_3w \tag{10a}$$

$$V=h_4u+h_5v+h_6w \tag{10b}$$

$$W=h_7u+h_8v+h_9w \tag{10c}$$

coefficients $h_1,h_2,\ldots,h_9$ are first-order transformation derivatives defined as

$$h_1=y_Yz_Z-y_Zz_Y \tag{11a}$$

$$h_2=z_Yx_Z-z_Zx_Y \tag{11b}$$

$$h_3=x_Yy_Z-x_Zy_Y \tag{11c}$$

$$h_4=y_Zz_X-y_Xz_Z \tag{11d}$$

$$h_5=z_Zx_X-z_Xx_Z \tag{11e}$$

$$h_6=x_Zy_X-x_Xy_Z \tag{11f}$$

$$h_7=y_Xz_Y-y_Yz_X \tag{11g}$$

$$h_8=z_Xx_Y-z_Yx_X \tag{11h}$$

$$h_9=x_Xy_Y-x_Yy_X \tag{11i}$$

and coefficients p_X, p_Y, and p_Z are second-order transformation derivatives defined as

$$p_X=c_1x_{XX}+c_2x_{YY}+c_3x_{ZZ}+c_4x_{XY}+c_5x_{YZ}+c_6x_{XZ} \tag{12a}$$

$$p_Y=c_1y_{XX}+c_2y_{YY}+c_3y_{ZZ}+c_4y_{XY}+c_5y_{YZ}+c_6y_{XZ} \tag{12b}$$

$$p_Z=c_1z_{XX}+c_2z_{YY}+c_3z_{ZZ}+c_4z_{XY}+c_5z_{YZ}+c_6z_{XZ} \tag{12c}$$

The determinant of the Jacobian transformation matrix is defined as

$$D=h_1x_X+h_4x_Y+h_7x_Z \tag{13}$$

The velocity components u,v,w are defined as

$$u=(h_1\phi_X+h_4\phi_Y+h_7\phi_Z)/D \tag{14a}$$

$$v=(h_2\phi_X+h_5\phi_Y+h_8\phi_Z)/D \tag{14b}$$

$$w=(h_3\phi_X+h_6\phi_Y+h_9\phi_Z)/D \tag{14c}$$

Equation (8) can be reduced to the two-dimensional equation derived in Ref. 7.

After the physical coordinates of grid points have been prescribed, the transformation derivatives $x_X,x_Y,x_Z,y_X\ldots$ $x_{XX},x_{XY},x_{YY}\ldots$ can be computed at each control point within a local mesh element. A second-order-accurate, finite difference approximation of the transformed full potential equation thus can be obtained by applying a second-order element (Fig. 1). Within the element, X, Y, and Z vary from -1 to 1 from nodal point to nodal point. Second-order shape functions then can be constructed that relate the function at any point p within the element to the values of the function at 27 nodal points. If the control point is chosen to be $X=Y=Z=0$, then the well-known second-order, centered, finite difference formulations are obtained. Detailed formulations can be found in Ref. 12 or 13.

Supersonic Flows and Shocks

The finite difference approximation to the full potential equation discussed thus far can be solved for flows that are entirely subsonic. To treat transonic flows, proper artificial viscosities or densities are normally added to the finite difference equation at supersonic points. The directional bias of supersonic flows can thus be reflected in the governing finite difference equation. At shock points, a shock-point operator is applied to represent the transition from a hyperbolic equation at supersonic points to an elliptic equation at subsonic points; it also determines the amount of numerical mass flux added at shocks to adjust their strength and location. The order of shock-point operator is at least one order lower than the order of the artificial viscosities, as will be shown later.

The second derivative of the potential function in the streamwise direction s is given as

$$\phi_{ss}=(1/q^2)(u^2\phi_{xx}+v^2\phi_{yy}+w^2\phi_{zz}+2uv\phi_{xy} +2vw\phi_{yz}+2uw\phi_{zz}) \tag{15}$$

Substituting Eqs. (1) and (2) into Eq. (15) yields

$$\phi_{ss}=(1/q^2)(U^2\phi_{XX}+V^2\phi_{YY}+W^2\phi_{ZZ}+2UV\phi_{XY} +2VW\phi_{YZ}+2UW\phi_{XZ}) \tag{16}$$

where U,V,W are given in Eq. (10).

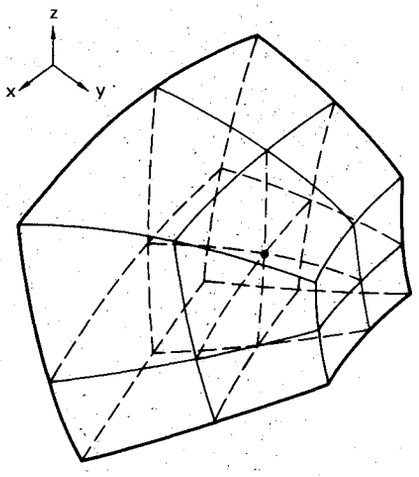

a) Physical space

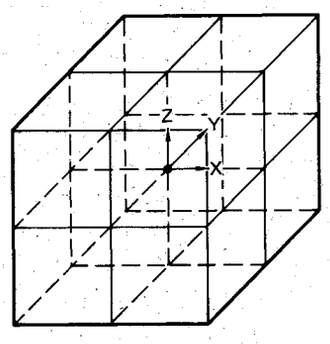

b) Computational space

Fig. 1 Transformation of a second-order element.

The directional bias of supersonic flows can be simulated properly by performing an upwind differencing or adding artificial viscosities in the approximate streamwise direction. If $Y=$const lines are in the approximate s direction, the principal part of ϕ_{ss} can be approximated by

$$\phi_{ss} \doteq \frac{U^2}{q^2}\phi_{XX} \tag{17}$$

A second-order artificial viscosity can be expressed as

$$H=\left[(\Delta X)^2\frac{\mu U^2\phi_{XX}}{D}\right]_{XX}=\left(\frac{\mu U^2\phi_{XX}}{D}\right)_{i-2} -2\left(\frac{\mu U^2\phi_{XX}}{D}\right)_{i-1}+\left(\frac{\mu U^2\phi_{XX}}{D}\right)_{i} \tag{18}$$

where

$$\mu=\max[1-(a^2/q^2),0] \tag{19}$$

H is then added to the finite difference representation of Eq. (8) at supersonic points. At shock points, i.e., the first downstream subsonic points after the shocks, the following first-order artificial viscosity H_s is added.

$$H_s=(p_m-1)\left[\frac{(\Delta X)\mu U^2\phi_{XX}}{D}\right]_X =\left[\left(\frac{\mu U^2\phi_{XX}}{D}\right)_{i-1}-\left(\frac{\mu U^2\phi_{XX}}{D}\right)_{i-2}\right](p_m-1) \tag{20}$$

where p_m is the parameter controlling nonconservative differencing. If $p_m=0$, the quantity $\mu U^2\phi_{XX}$ is conserved along $Y=$const lines, implying that the added artificial viscosities are conserved along approximate streamlines. If $p_m>0$, a numerical mass flux is introduced at shocks, modifying the locations and strengths of the shocks. The effect of p_m on the captured shocks will be discussed later. Although μ is a ramp function, both H and H_s reduce to zero as the mesh size goes to zero. In many existing schemes, zeroth-order artificial viscosities are added at shock points; however it has been shown in Ref. 11 that a zeroth-order error will appear at the shock, and poor resolution of the solution will result. Therefore, it is important to model H_s properly at shocks. The present solution is second-order accurate at both subsonic and supersonic points, and first-order accurate at shock points. The scheme is second-order quasiconservative. In the so-called quasiconservative schemes, only the differencing of artificial viscosities is in divergence form; the differencing of the governing potential equation is not. A second-order fully conservative scheme also can be constructed by incorporating H and H_s into an existing finite volume algorithm.[1]

Third-order, quasiconservative and fully conservative schemes can be developed by adding the following third-order artificial viscosity at supersonic points.

$$H=\left[\frac{(\Delta X)^3\mu U^2\phi_{XX}}{D}\right]_{XXX}=\left(\frac{\mu U^2\phi_{XX}}{D}\right)_i-3\left(\frac{\mu U^2\phi_{XX}}{D}\right)_{i-1} +3\left(\frac{\mu U^2\phi_{XX}}{D}\right)_{i-2}-\left(\frac{\mu U^2\phi_{XX}}{D}\right)_{i-3} \tag{21}$$

and adding the following second-order artificial viscosity at shock points.

$$H_s=(p_m-1)\left[\frac{(\Delta X)^3\mu U^2\phi_{XX}}{D}\right]_{XX}=\left[\left(\frac{\mu U^2\phi_{XX}}{D}\right)_{i-3} -2\left(\frac{\mu U^2\phi_{XX}}{D}\right)_{i-2}+\left(\frac{\mu U^2\phi_{XX}}{D}\right)_{i-1}\right](p_m-1) \tag{22}$$

If p_m is set to zero, the quantity $\mu U^2\phi_{XX}$ is conserved along $Y=$const lines. If p_m is set to be greater than zero, a numerical mass flux is added at shocks, as in the second-order schemes.

Grid Generation and Computational Domain

The finite difference approximation of the governing equation obtained in the previous section can be constructed with the knowledge of mesh-point locations. The coordinate transformation derivatives are found at each control point within a local second-order element shown in Fig. 1. Any scheme that generates a grid system in a regular computational domain can be incorporated into the finite difference flow equation solver.

In the present study, a grid-generation scheme developed in Ref. 14 is applied. The transformation of the physical space to the computational space is shown in Fig. 2. The computational space is truncated at a finite distance from the wing surface. For the results presented here, the far-field boundary is placed approximately five to six root-chord lengths from the wing surface in the streamwise and surface normal directions, and the spanwise far field is located two to three semispan lengths from the wing tip and the outboard far field. A surface about which the mesh is unwrapped extends between the wing tip and the far field boundary. C-type meshes are generated which wrap around the fuselage nose and wing leading edge. Details of the grid-generation scheme can be found in Ref. 14 and will not be duplicated here. Typical grids used in the present calculation are presented in Figs. 3 and 4. Figure 3 shows the grid distribution on an ONERA-M6 wing on a vertical wall, and Fig. 4 shows the grid distribution on the same wing on a semi-infinite cylinder.

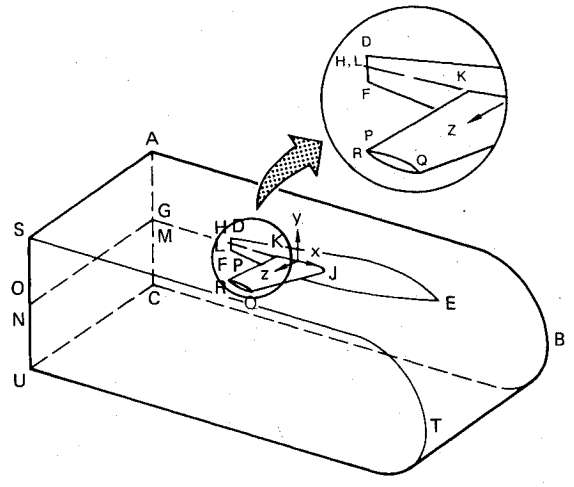

a) Physical space

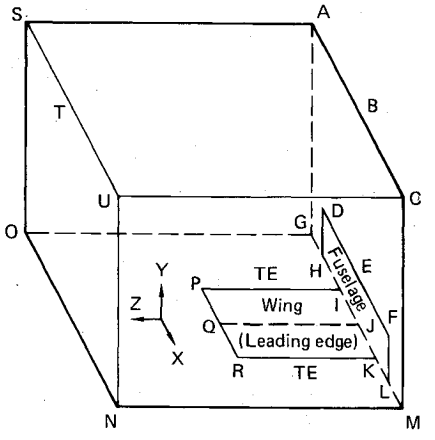

b) Computational space

Fig. 2 Physical and computational domain for a wing-fuselage configuration.

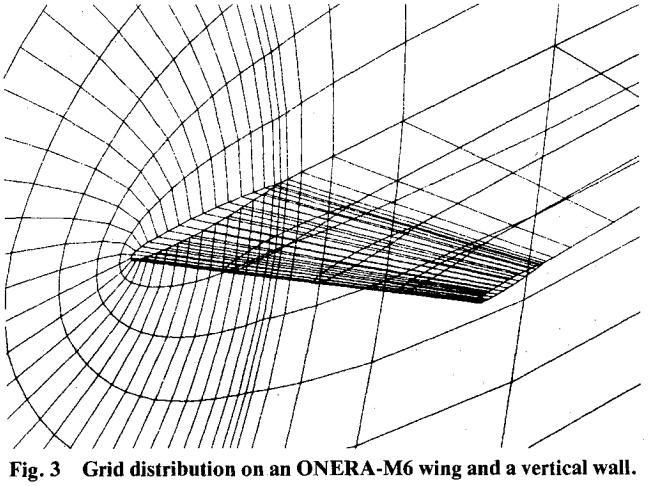

Fig. 3 Grid distribution on an ONERA-M6 wing and a vertical wall.

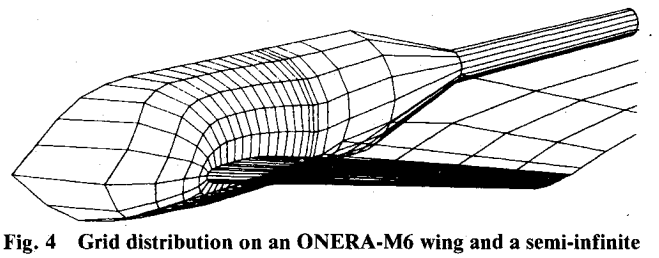

Fig. 4 Grid distribution on an ONERA-M6 wing and a semi-infinite fuselage.

Boundary Conditions

The necessary boundary conditions include the impermeability condition on the wing and fuselage surfaces, the Kutta condition along the trailing edge, the zero streamwise variation on the downstream Trefftz plane, and the freestream condition on the other far-field boundaries. For easy implementation of the far-field freestream condition, a reduced potential G, representing a perturbation from the freestream, is introduced according to

$$\phi = U_\infty (x\cos\alpha + y\sin\alpha + G) \tag{23}$$

where U_∞ is the freestream velocity and α the angle of attack.

On the boundary cross planes, ACUSA and SUNOS (Fig. 2) G is set to zero, representing the freestream condition. On the Trefftz plane or the boundary cross plane AGOSA and CMNUC, the streamwise variations are assumed to be zero, therefore, the following two-dimensional equation is applied.

$$c_2\phi_{YY} + c_3\phi_{ZZ} + c_5\phi_{YZ} + c_8\phi_Y + c_9\phi_Z = 0 \tag{24}$$

Equation (24) is obtained from Eq. (8) by neglecting all derivatives in the X direction.

On the fuselage and wing surfaces, the impermeability condition is applied

$$V = 0, \text{ on the wing surface} \tag{25}$$

and

$$W = 0, \text{ on the fuselage surface} \tag{26}$$

Exact surface-boundary conditions can be enforced at boundary points by substituting Eqs. (10b) and (10c) into Eqs. (25) and (26), respectively, and solving the equations for the value of the potential function at boundary points. One-sided differencing is used in the surface-normal direction so that there is no need to extrapolate the potential to imaginary points inside the wing or fuselage surfaces. However, Eq. (26) might not be suitable for highly distorted grids near the fuselage and wing intersection. Boundary conditions obtained from the finite volume algorithm[1] give better results near the intersection. Therefore, all solutions presented in the subsequent section were obtained by applying the finite volume surface-boundary condition in the cross plane ACMG.

Along the trailing edge, the linearized equation

$$(h_1^2 + h_2^2 + h_3^2)\phi_{XX} + (h_4^2 + h_5^2 + h_6^2)\phi_{YY} + (h_7^2 + h_8^2 + h_9^2)\phi_{ZZ} = 0 \tag{27}$$

is assumed to hold. Equation (27) is obtained from Eq. (8) by neglecting the nonlinear velocity contribution and the cross and first-derivative terms. This linearized equation is approximately valid along the trailing edge only for wing cross sections having a finite trailing-edge angle where zero flow velocity can be approximately assumed; Eq. (27) can be regarded as an interpolation operator when the wing trailing edge is cusped. The circulation Γ at each spanwise location is determined iteratively as the solution proceeds. Constant discontinuities in potential across the cut downstream of the trailing edge are enforced along the streamwise coordinate lines extending from the trailing edge to the downstream far field. The value of the discontinuity in each spanwise plane is computed at the trailing edge by satisfying Eq. (27) at both the upper and lower trailing edges.

Along the wing tip, the surface boundary condition is difficult to enforce because of the type of grids used; therefore, the potential function along the tip is not calculated exactly. To avoid directly using the potential function along

the tip in the calculation of spanwise derivatives, the relation, $\phi_{YY}=0$ is solved at points just outboard of the tip on the surface about which the mesh is unwrapped. This method is used in treating the surface of the vortex sheet in the FLO-22 code.[15]

Relaxation Strategies

The finite difference approximation to Eq. (8) can be solved by a line-relaxation scheme with the boundary conditions described in the previous section. To ensure that the relaxation scheme corresponds to a convergent process, the old and updated values of the potential functions, ϕ and ϕ^+, must be mixed properly. The basic relaxation strategies developed for the present method are similar to the ones described in Refs. 12 and 16, except for careful treatment of artificial viscosities at supersonic and shock points.

In the second-order quasiconservative scheme, the old and new values of ϕ contributing to the terms $(q^2-a^2)\phi_{ss}+H$ (or H_s) of the relaxation equation are chosen to ensure a convergent process in the $i=$ const line sweep according to

$$(q^2-a^2)\phi_{ss}+H=\left[\left(\frac{\mu U^2}{D}\right)_{i,j,k}+\left(4\frac{\mu U^2}{D}\right)_{i-m,j,k}+\left(\frac{\mu U^2}{D}\right)_{i-2m,j,k}\right](c_{i,j,k}-c_{i-m,j,k})$$
$$-2\left[\left(\frac{\mu U^2}{D}\right)_{i-m,j,k}+\left(\frac{\mu U^2}{D}\right)_{i-2m,k}\right](c_{i,j,k}-c_{i-2m,j,k})+R_{ss} \tag{28}$$

for supersonic points, and

$$(q^2-a^2)\phi_{ss}+H_s=\mp\left[2\left(\frac{\mu U^2}{D}\right)_{i-m,j,k}+\left(\frac{\mu U^2}{D}\right)_{i-2m,j,k}\right]\times(1-p_m)(c_{i,j,k}-c_{i-m,j,k})-\left[\left(\frac{\mu U^2}{D}\right)_{i-m,j,k}$$
$$-2\left(\frac{\mu U^2}{D}\right)_{i-2m,j,k}\right](1-p_m)(c_{i,j,k}-c_{i-2m,j,k})+R_{ss} \tag{29}$$

for shock points. The index m is equal to 1 and -1 for positive and negative U, respectively, $c_{i,j,k}=\phi^+_{i,j,k}-\phi_{i,j,k}$ is the correction to the potential function and R_{ss} is the residual of the finite difference approximation to $(q^2-a^2)\phi_{ss}$ evaluated using old values of ϕ. The second-order fully conservative scheme applies the same strategy to treat the artificial viscosities at supersonic and shock points. A similar strategy also can be developed for the third-order quasiconservative and fully conservative schemes.

Numerical Results

Typical solutions obtained using the second- and third-order, quasiconservative and fully conservative schemes are presented in this section. Two meshes are used in all calculations. The coarse mesh contains 44 mesh cells in the X direction, 10 mesh cells in the Y direction, and 7 mesh cells in the Z direction; 32×5 mesh cells are on the unwrapped wing surface. The fine mesh has double the number of mesh cells in each direction. Two hundred relaxation sweeps were performed on the coarse mesh, followed by two hundred relaxation sweeps on the fine mesh.

Figures 5 and 6 present comparisons of first- and second-order fully conservative solutions obtained for the ONERA-M6 wing on a semi-infinite fuselage shown in Fig. 4. The fuselage has a constant radius of 0.2 semispan length, measured from the wing root to wing tip, in the section of wing-fuselage conjunction. There are no experimental data for this configuration; however, experimental data are

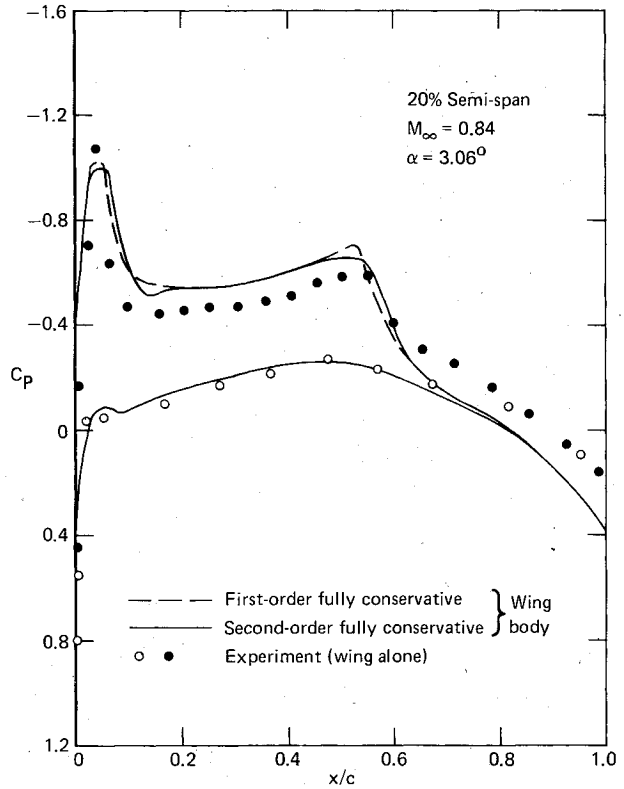

Fig. 5 Comparison of first- and second-order fully conservative solutions at 20% semi-span.

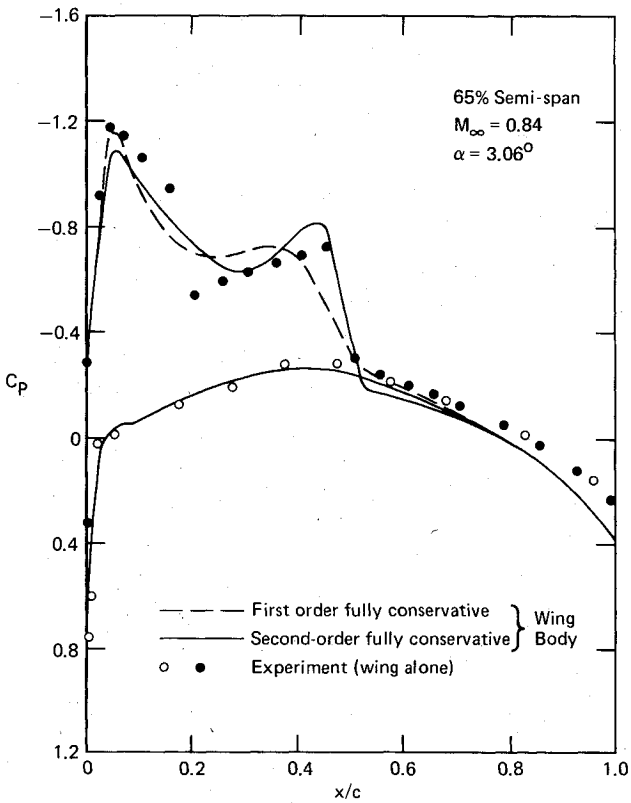

Fig. 6 Comparison of first- and second-order fully conservative solutions at 65% semi-span.

available for the same wing on a vertical wall in Ref. 17. Computed solutions at 20 and 65% semispan locations are presented in Figs. 5 and 6, respectively, for $M_\infty=0.84$ and $\alpha=3.06$ deg where α is the angle of attack and also the angle of incidence between the wing and fuselage. The fuselage

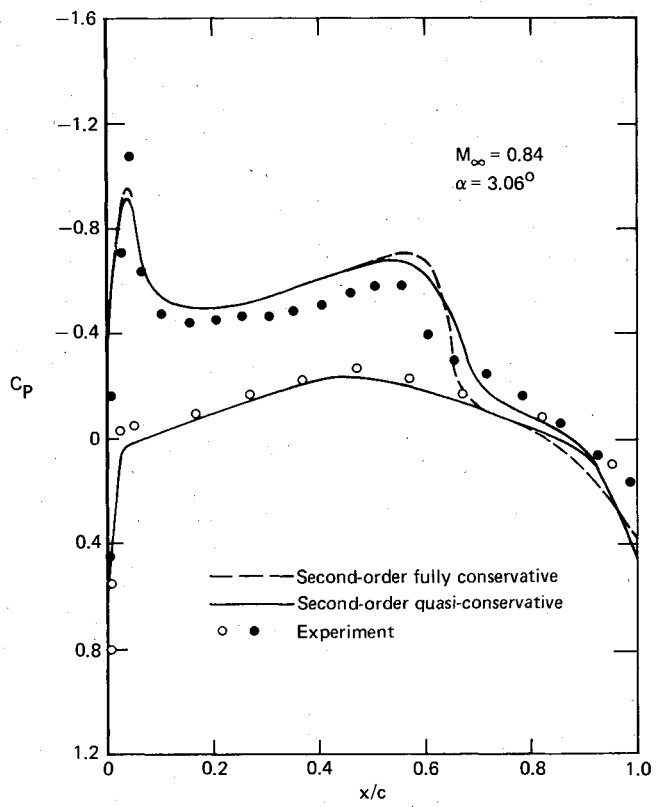

Fig. 7 Second-order solutions for an ONERA-M6 wing on a wall at the 20% semispan location.

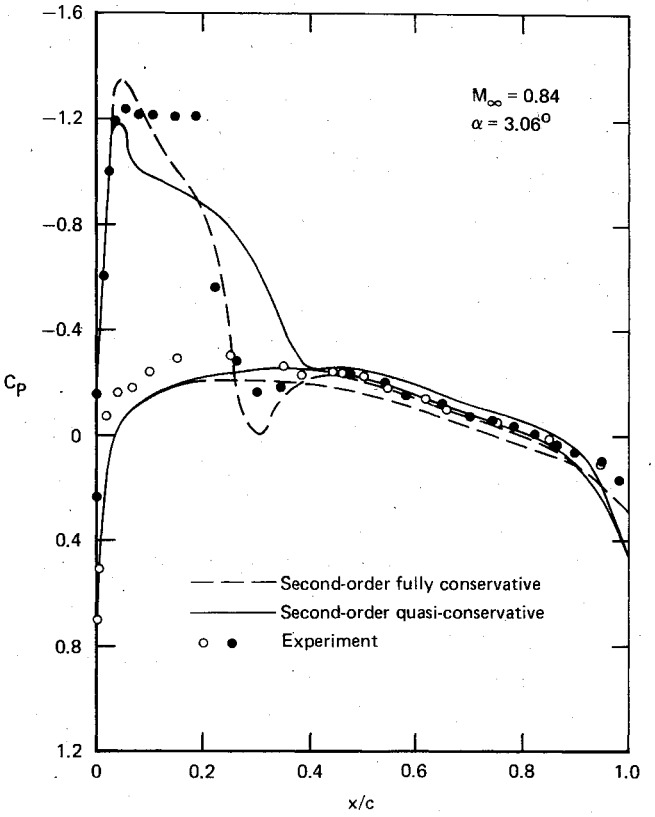

Fig. 9 Second-order solutions for an ONERA-M6 wing on a wall at the 95% semispan location.

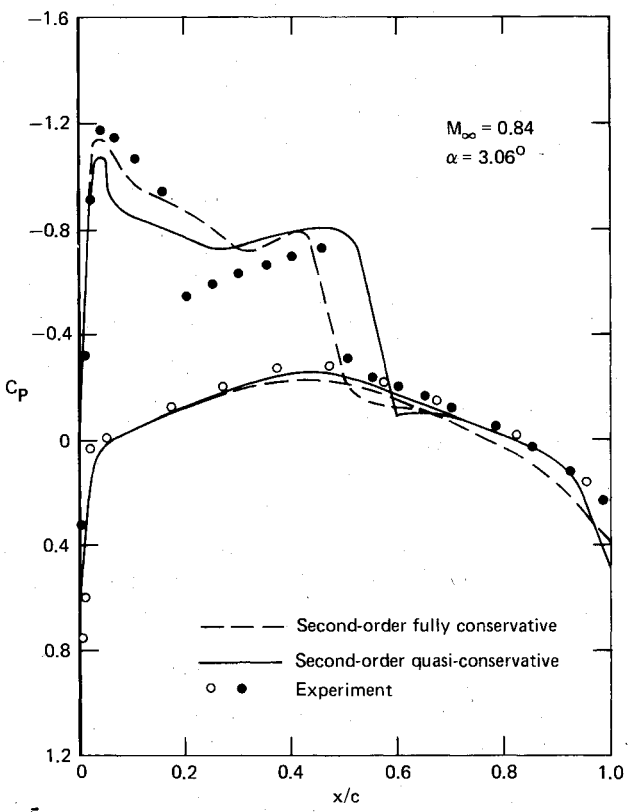

Fig. 8 Second-order solutions for an ONERA-M6 wing on a wall at the 65% semispan location.

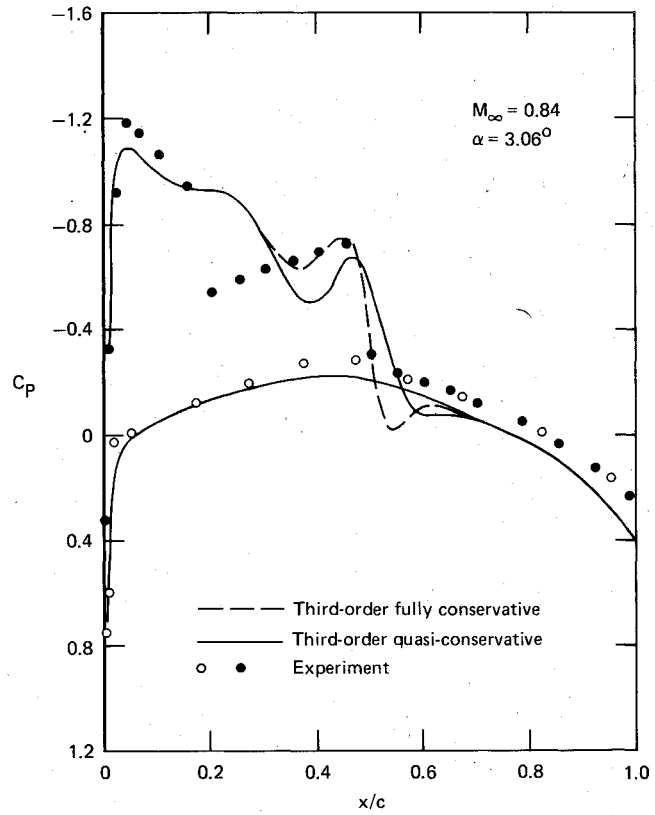

Fig. 10 Comparison of third-order quasiconservative and fully conservative solutions at the 65% semispan location.

effect is not pronounced in this case, and agreement between the computed solutions and experiments is generally good. At the 20% semispan location, the first-order solution agrees with the second-order solution except for minor differences in suction peaks and details at the shocks. At the 65% semispan location, experimental data show a distinct double shock on the upper surface. The second-order solution obviously resolves this double shock better than the first-order solution, although there are still small discrepancies between the second-order solution and experiments, presumably because the mesh used for the computation is relatively coarse.

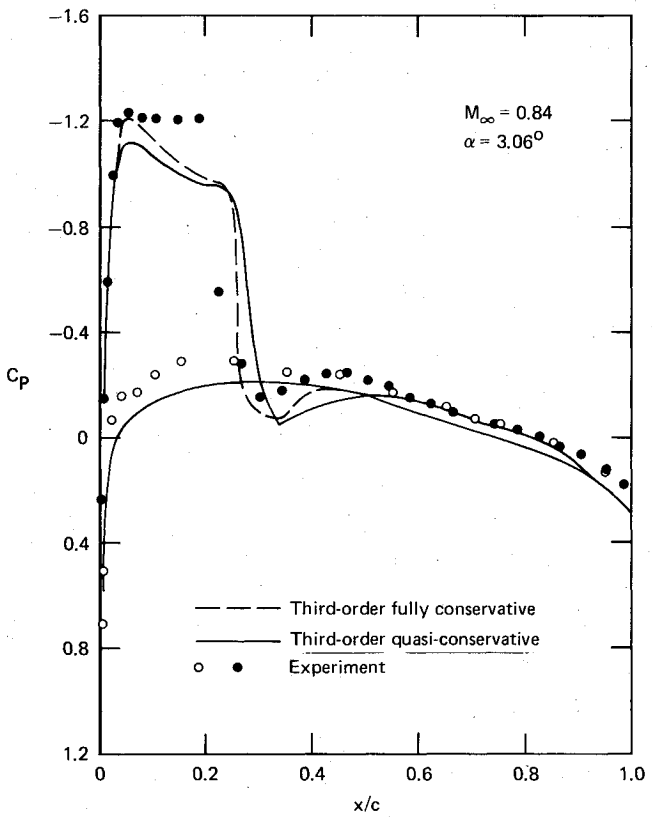

Fig. 11 Comparison of third-order quasiconservative and fully conservative solutions at the 95% semispan location.

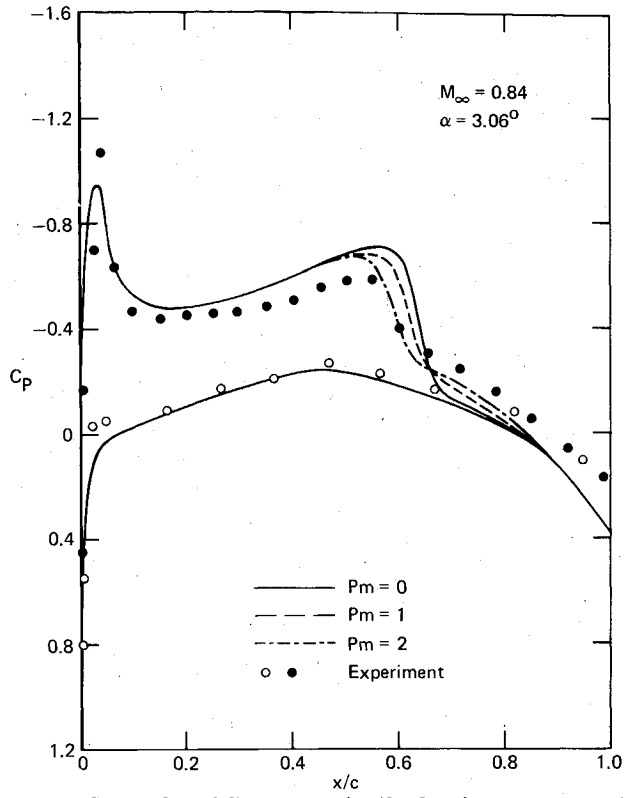

Fig. 12 Study of partially conservative shock-point operators at the 20% semispan location on an ONERA-M6 wing.

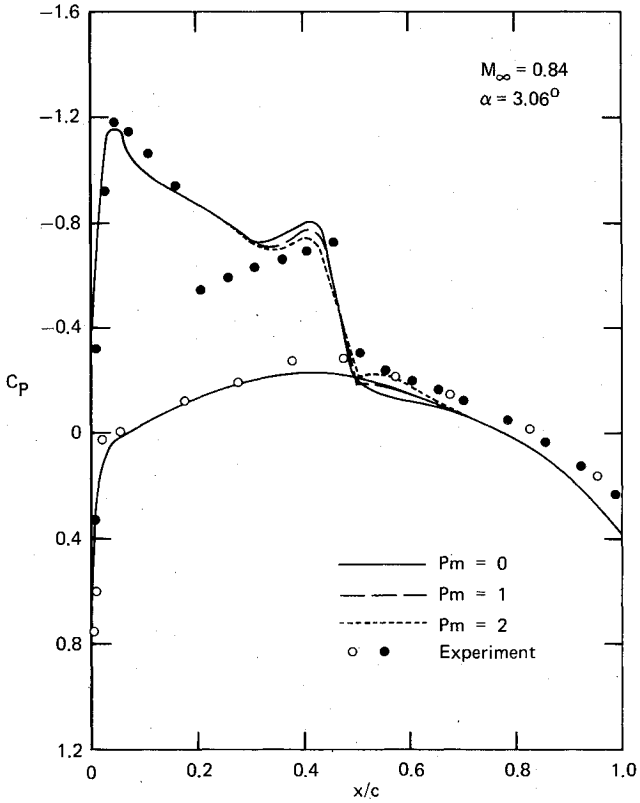

Fig. 13 Study of partially conservative shock-point operators at the 65% semispan location on an ONERA-M6 wing.

In Figs. 7-11 pressure distributions obtained for an ONERA-M6 wing on a wall, Fig. 3, are shown and compared with experimental data.[16] The freestream Mach number is 0.84 and the angle of attack is 3.06 deg. Second-order quasiconservative and first- and second-order fully conservative solutions were obtained at the 20, 65, and 95% semispan locations and are shown in Figs. 7-9. At the 20% semispan location, numerical solutions predict lower suction peaks. The plateau pressures at the 20 and 65% semispan locations are slightly overpredicted, while the pressures downstream of the shocks are slightly higher than the experimental data. The locations of shocks are predicted quite accurately by the numerical solutions. Although the mesh used is still relatively coarse, the overall agreement between the numerical and experimental results is satisfactory. The quasiconservative solutions predict a more positive pressure at the trailing edge and yield better agreement with the experimental data upstream of the trailing edge. This apparently is due to the enforcement of the exact surface boundary condition and the linearized equation, Eq. (27), which approximately simulates a flow stagnation condition for finite trailing-edge angles, as mentioned previously. However, the quasiconservative solutions predict a further downstream shock location at 65% semispan and do not resolve the suction peak as well as the fully conservative scheme. The poor resolution of the suction peak is caused by the second-order element not resolving the surface curvature and potential gradient near the leading edge as the exact surface-boundary condition is enforced. The leading-edge resolution can be significantly improved by using a third-order element, as shown in Ref. 7.

Third-order quasiconservative and fully conservative solutions are obtained for the same wing and compared with experiment in Figs. 10 and 11 at the 65 and 95% semispan locations, respectively. The finite volume boundary conditions were applied on the airfoil surface for both solutions. The pressure distributions in the supersonic region are more accurately predicted at the 95% semispan location than in the second-order solution shown in Fig. 7, although the plateau pressure still is underpredicted. A triple shock pattern is observed in the computed pressure distribution at the 65% semispan location, although the first shock is somewhat ambiguous. This pattern also appears at spanwise locations

between 50 and 70%. Evidence of the triple shock is not shown in the experimental data; however, triple-shock structures have been observed in static pressure distributions obtained with other wings at transonic speeds. This feature probably is not associated with poor convergence, since the solutions presented here have all converged to sufficiently small residuals. It is also possible that the triple-shock pattern is the result of a numerical oscillation caused by interaction between the numerical frequency of the third-order artificial viscosity and the wave frequency associated with the double shock. Finer mesh solutions are needed to explain the characteristics of the third-order solutions.

A study of the shock-point operator for the same ONERA-M6 wing on the wall at $M_\infty = 0.84$ and $\alpha = 3.06$ is shown in Figs. 12 and 13. As mentioned previously, p_m is the parameter controlling the nonconservative differencing of the shock-point operators in Eqs. (20) and (22). Solutions are obtained for $p_m = 0$, 1, and 2 at 20 and 65% semispan locations by using the second-order artificial viscosity at supersonic points. A second-order fully conservative solution is obtained with $p_m = 0$. As p_m increases, the amount of nonconservative differencing increases, and the additional mass flux introduced at the shock increases. By adjusting the value of p_m, part of shock induced boundary-layer displacement effect can be simulated. By increasing the value of p_m, the shock moves upstream, the shock strength reduces, and agreement of the computed pressure with experimental data is significantly improved both upstream and downstream of the shocks. Solutions obtained by setting $p_m = 2$ seems to yield best agreement with experiments.

Conclusions

Second- and third-order fully conservative and quasi-conservative schemes have been developed to compute flowfields about transonic wings and wing-body configurations. The quasiconservative scheme was developed by solving a finite difference representation of a transformed full potential equation formulated in this paper and enforcing an exact body surface boundary condition.

The second-order solutions obtained have been shown to provide better solution resolution for a double shock than the conventional first-order schemes. The third-order solutions show a triple-shock pattern. Additional study will be required to determine whether this pattern is a real flowfield characteristic or a feature of the numerical scheme. The enforcement of an exact surface-boundary condition in the quasiconservative scheme provides solutions with better agreement with experiments upstream of the trailing edge.

A special shock-point operator is introduced to control the amount of nonconservative differencing at shock points and thus modify the location and strength of shocks. Proper choice of the shock-point operator significantly improves the agreement of computed pressure distribution with experimental data near the shocks.

Acknowledgments

This work was supported by David W. Taylor Naval Ship Research and Development Center under Contract N000167-81-C-0057. Helpful discussions with Professor D. A. Caughey are gratefully acknowledged.

References

[1] Jameson, A. and Caughey, D. A., "A Finite-Volume Method for Transonic Potential Flow Calculations," *Proceedings of AIAA 3rd Computational Fluid Dynamics Conference,* Albuquerque, New Mex., June 1977, pp. 35-54.

[2] Caughey, D. A. and Jameson, A., "Progress in Finite-Volume Calculations for Wing-Fuselage Combinations," *AIAA Journal,* Vol. 18, Nov. 1980, pp. 1281-1288.

[3] Chmielewski, G. E., "Transonic Wing/Body Flow Analysis Using Non-Surface-Fitted Coordinates," AIAA Paper 81-0384, Jan. 1981.

[4] Bailey, F. R. and Ballhaus, W. F., "Relaxation Methods for Transonic Flow About Wing-Cylinder Combinations and Lifting Swept Wings," *Lecture Notes in Physics,* Vol. 19, Springer-Verlag, 1972, pp. 3-9.

[5] Boope, C. W., "Computational Transonic Flow About Realistic Aircraft Configurations," AIAA Paper 78-104, Jan. 1978.

[6] Jameson, A., "Transonic Potential Flow Calculations Using Conservative Form," *Proceedings of AIAA 2nd Computational Fluid Dynamics Conference,* Hartford, Conn., June 1975, pp. 148-161.

[7] Chen, L. T., "Improved Finite-Difference Scheme for Transonic Airfoil Flowfield Calculations," *AIAA Journal,* Vol. 20, Feb. 1982, pp. 218-226.

[8] Ives, D. C. and Liutermoza, J. F., "Second-Order-Accurate Calculation of Transonic Flow Over Turbomachinery Cascades," *AIAA Journal,* Vol. 17, Aug. 1979, pp. 870-876.

[9] Caughey, D. A. and Jameson, A., "Basic Advances in the Finite Volume Method for Transonic Potential Flow Calculations," *Proceedings of Symposium on Numerical and Physical Aspects of Aerodynamic Flows,* edited by T. Cebeci, 1981.

[10] Jameson, A., "Acceleration of Transonic Potential Flow Calculations on Arbitrary Meshes by the Multiple Grid Methods," *Proceedings of AIAA 4th Computational Fluid Dynamics Conference,* Williamsburg, Va., July 1979, pp. 122-146.

[11] Chen, L. T. and Caughey, D. A., "On Various Treatments of Potential Equations at Shocks," Numerical Boundary Condition Procedures, NASA-CP-2201, Moffett Field, Calif., Oct. 1981, pp. 121-138.

[12] Chen, L. T. and Caughey, D. A., "Calculation of Transonic Inlet Flowfields Using Generalized Coordinates," *Journal of Aircraft,* Vol. 17, March 1980, pp. 167-174.

[13] Chen, L. T. and Caughey, D. A., "Higher-Order Finite-Difference Scheme for Three-Dimensional Transonic Flowfields About Axisymmetric Bodies," *Journal of Aircraft,* Vol. 17, Sept. 1980, pp. 668-676.

[14] Chen, L. T., Caughey, D. A., and Verhoff, A., "A Nearly Conformal Grid-Generation Method for Transonic Wing-Body Flowfield Calculation," AIAA Paper 82-0108, Jan. 1982.

[15] Jameson, A. and Caughey, D. A., "Numerical Calculation of the Transonic Flow Past a Swept Wing," ERDA Research and Development Rept. C00-3077-140, Mathematical Sciences, New York University, June 1977.

[16] Jameson, A., "Iterative Solution of Transonic Flows Over Airfoils and Wings, Including Flows at Mach 1," *Communications on Pure and Applied Mathematics,* Vol. 27, 1974, pp. 283-309.

[17] Schmitt, V. and Charpin, F., "Pressure Distributions on the ONERA-M6 Wing at Transonic Mach Numbers; in Experimental Data Base for Computer Program Assessment," AGARD-AR-138, May 1979.